Research Article

Dingshan Zheng, Hailu Wang, Ruoling Chen, Long Li, Jiaxiang Guo, Yue Gu, Muhammad M. Zubair, Xiangxiang Yu, Long Jiang, Desheng Zhu, Yan Xiong, Han Zhang, Wen-Xing Yang* and Jinshui Miao*

High-detectivity tin disulfide nanowire photodetectors with manipulation of localized ferroelectric polarization field

Abstract: Tin sulfide semiconductor nanowires (NWs) have been widely investigated for photodetection applications because of their good optical and electrical properties. Herein, we synthesized n-type SnS_2 NWs and then fabricated SnS_2 NW photodetectors with a ferroelectric polymer side-gate. The strong electric field induced by ferroelectric polymer can effectively suppress the dark current and improve the detectivity in SnS_2 NW photodetectors. The photodetectors after polarization depletion exhibit a high photoconductive gain of 4.0×10^5 and a high responsivity of 2.1×10^5 A W^{-1}. Compared with devices without polarization depletion, the detectivity of polarization-depleted photodetectors is improved by at least two orders of magnitude, and the highest detectivity is 1.3×10^{16} Jones. Further, the rise and fall time are 56 and 91 ms respectively, which are about tens of times faster than those without polarization depletion. The device also shows a good spectral response from ultraviolet to near-infrared. This study demonstrates that ferroelectric materials can enhance optoelectronic properties of low-dimensional semiconductors for high-performance photodetectors.

Keywords: ferroelectric; nanowire; photodetector; SnS_2.

Dingshan Zheng, **Hailu Wang**, and **Ruoling Chen** are equally contributed to this work.

***Corresponding authors: Wen-Xing Yang,** School of Physics and Optoelectronic Engineering, Yangtze University, Jingzhou 434023, China, E-mail: wenxingyang2@126.com; **Jinshui Miao,** State Key Laboratory of Infrared Physics, Shanghai Institute of Technical Physics, Chinese Academy of Sciences, Shanghai 200083, China, E-mail: jsmiao@mail.sitp.ac.cn. https://orcid.org/0000-0001-6050-5578 (W.-X. Yang)
Dingshan Zheng, Ruoling Chen, Long Li, Xiangxiang Yu, Long Jiang, Desheng Zhu and Yan Xiong, School of Physics and Optoelectronic Engineering, Yangtze University, Jingzhou 434023, China, E-mail: dszheng82@163.com (D. Zheng), 201971165@yangtzeu.edu.cn (R. Chen), lilong202071205@163.com (L. Li), yuxx518@126.com (X. Yu), jianglong@yangtzeu.edu.cn (L. Jiang), dszhu@yangtzeu.edu.cn (D. Zhu), xiongyan1215@163.com (Y. Xiong). https://orcid.org/0000-0003-4060-2228 (D. Zheng)
Hailu Wang, Jiaxiang Guo, Yue Gu and Muhammad M. Zubair, State Key Laboratory of Infrared Physics, Shanghai Institute of Technical Physics, Chinese Academy of Sciences, Shanghai 200083, China, E-mail: wanghailu17@mails.ucas.ac.cn (H. Wang), guojiaxiang@mail.sitp.ac.cn (J. Guo), guyue@mail.sitp.ac.cn (Y. Gu), zubair@hnu.edu.cn (M.M. Zubair)
Han Zhang, Institute of Microscale Optoelectronics, College of Physics and Optoelectronic Engineering, Shenzhen University, Shenzhen 518060, China, E-mail: hzhang@szu.edu.cn. https://orcid.org/0000-0002-9131-9767

1 Introduction

One-dimensional semiconductor NWs have been intensively studied for room-temperature photodetection with high sensitivity, gain and wide spectral response, etc. [1–6]. IV−VI chalcogenide tin sulfide semiconductors, including SnS [7–10] and SnS_2 [11–14] shows tremendous potential in optoelectronic applications because of their narrow bandgap, high carrier mobility and light−matter coupling efficiency, etc. [9, 11]. For example, p-type SnS NWs have been synthesized and demonstrated excellent optoelectronic performance in our previous work [7]. SnS_2 is an n-type semiconductor with bandgap ranging from 2.1 to 2.4 eV [11, 15], and SnS_2-based nanostructures have been demonstrated to show broad prospects in field-effect transistors [14, 15], battery materials [16, 17], photodetectors [12, 13, 18], gas sensors [19], and solar cells [20, 21]. Most studies on SnS_2 nanostructures mainly focus on quantum dots [22], nanosheets [12, 13, 18] and thin films [23, 24], but very limited study on SnS_2 NWs. Thus, it is essential to explore 1D SnS_2 NWs and their optoelectronic properties. In addition, whether it is an n-type or p-type NW photodetector, its optoelectronic performances have been greatly

improved compared with traditional photodetectors. However, the large dark current is still a major problem to be solved, and it is necessary to improve these problems by designing a certain device structure or changing certain conditions of the photodetector.

In this work, we synthesized SnS$_2$ NWs by the CVD method. To suppress the dark current caused by defect/trap induced carriers and improve the detectivity of photodetectors, we integrated ferroelectric polymer side-gate with SnS$_2$ NW. The intrinsic carriers in the SnS$_2$ NW channel can be depleted by ultrahigh electrostatic field induced by the polarization of ferroelectric polymer. Therefore, the background current is suppressed to as low as 10^{-12} A. Furthermore, the detectivity is increased by at least two orders of magnitude, and the rise and fall time are improved by tens of times. The noise characteristics show that the device has low noise equivalent power (NEP) and noise current (the frequency noise current power is ~6.9×10^{-28} A^2 and 1/f noise current is ~2.6×10^{-14} A, respectively). The SnS$_2$ NW photodetectors after polarization depletion exhibit a high photoconductive gain of 4.0×10^5, a high responsivity of 2.1×10^5 A W^{-1} and ultra-high detectivity of 1.3×10^{16} Jones.

2 Experimental section

2.1 Nanowires synthesis and characterization

In this work, the SnS$_2$ NWs were synthesized in a tube furnace via the CVD method. The high-purity SnS$_2$ powder (0.1 g) was put at the heating zone center as source material and S powder (0.1 g) was put upstream of the central temperature zone to the SnS$_2$ powder at a distance of ~15 cm. The Au film with a thickness of 1 nm was pre-deposited onto the Si substrate as the catalyst. The substrate was put downstream approximately 12 cm away from the SnS$_2$ powder. A carrier gas mixture of argon and hydrogen (10%) of 100 sccm was introduced into the tube. Then the temperature of the SnS$_2$ powder was heated rapidly to 760 °C and kept at this temperature for 30 min. After that, the furnace was cooled naturally to room temperature under carrier gas flow. Scanning electron microscope (SEM), X-ray diffraction (XRD), high-resolution transmission electron microscopy (HR-TEM), and energy-dispersive X-ray spectroscopy (EDS) characterizations were performed to determine the crystal properties, diameter, elemental composition of as-synthesized SnS$_2$ NWs together.

2.2 Photodetectors fabrication and characterization

The field-effect transistors (FETs) on the basis of single SnS$_2$ NW can be assembled by electron-beam lithography (EBL). The SnS$_2$ NWs were first dispersed by contact and physically transferred onto Si/SiO$_2$ substrate with marks, following by spin-coating with MMA and PMMA. EBL with an NPGS system (JEOL 6510) was used to determine the drain and source electrodes. Before metallization, the SnS$_2$ NWs were

immersed in diluted HF (2%) solution for 15 s to eliminate the surface oxide layer. The Cr/Au (15 nm/60 nm) electrodes were completed through vacuum thermal evaporation and stripping. A ferroelectric polymer poly(vinylidene fluoride-trifluoroethylene) [P(VDF-TrFE)] with 300 nm in thickness was placed on the SnS$_2$ NW devices through the spin-coating method. Then the P(VDF-TrFE) film was annealed at 150 °C for 3 h to enhance its crystallinity. The electrical and opto-electronic measurements of the SnS$_2$ NW FETs were conducted with the vacuum probe station (Lake Shore TTPX) and semiconductor parameter analyzer (Keithley 4200). The time-resolved response measurements were conducted by periodically turning on and off the laser and monitored by a digital oscilloscope. Noise power spectra measurements were performed by a noise measurement system (NC300).

3 Results and discussion

The SEM image of SnS$_2$ NWs is displayed in Figure 1a showing a uniform structure with a length of tens of micrometers and a diameter of 30–200 nm. Figure 1b shows the HR-TEM image of single SnS$_2$ NW and the corresponding SAED pattern indicating that the SnS$_2$ NW has a single-crystalline architecture at the [001] direction and lattice distance of 0.296 nm. The XRD (Figure 1c) and EDS (Figure 1d) characterizations also conform to the previous studies [25]. The XRD spectrum of SnS$_2$ NWs shows all main diffraction peaks at $2\theta \sim 15.0°$, 28.3°, 32.0°, 42.0°, 50.0°, 52.5°, 58.4°, corresponding to (001), (100), (101), (102), (110), (111) and (200) planes (JCPDS No. 23-0677). The EDS spectrum of the sample shows that there are elements such as C, O, Cu, Si, S and Sn, in which the presence of C and Cu is caused by the carbon micro gate substrate, while O is the oxide layer of the sample surface.

To investigate the photodetection characteristics of SnS$_2$ NWs, back-gated SnS$_2$ NW FETs were fabricated, as shown in Figure 2a. Figure 2b shows the I_{ds}–V_{gs} transfer characteristics of the device for various V_{ds} and the linear I_{ds}–V_{gs} transfer characteristic at $V_{ds} = 1$ V is displayed in Figure 2c. The SnS$_2$ NW FETs exhibit typical n-type transistor behavior with a high current on-off ratio of 10^7 at $V_{ds} = 1$ V. The electron mobility μ_{FE} of single SnS$_2$ NW FET is calculated using the expression: $\mu_{FE} = g_m L^2/(C_g V_{ds})$ [26, 27], where $g_m = dI_{ds}/dV_{gs}$ is the transconductance and C_g is the capacitance of back-gated FET. C_g can be estimated on the basis of the cylinder on-plane model [26]: $C_g = 2\pi\varepsilon_0\varepsilon_r L/[\ln(4h/d)]$, where ε_0 is free space permittivity, ε_r is the dielectric constant of SiO$_2$, $h = 110$ nm is the thickness of the SiO$_2$ layer, $L = 3$ μm is the length of the channel, $d = 90$ nm is the diameter of SnS$_2$ NW (see the inset in Figure 3d). The calculated μ_{FE} is ~131.8 cm^2 V^{-1} s^{-1} at $V_{ds} = 1$ V. The electron mobility of the SnS$_2$ NW FET is comparable with that of
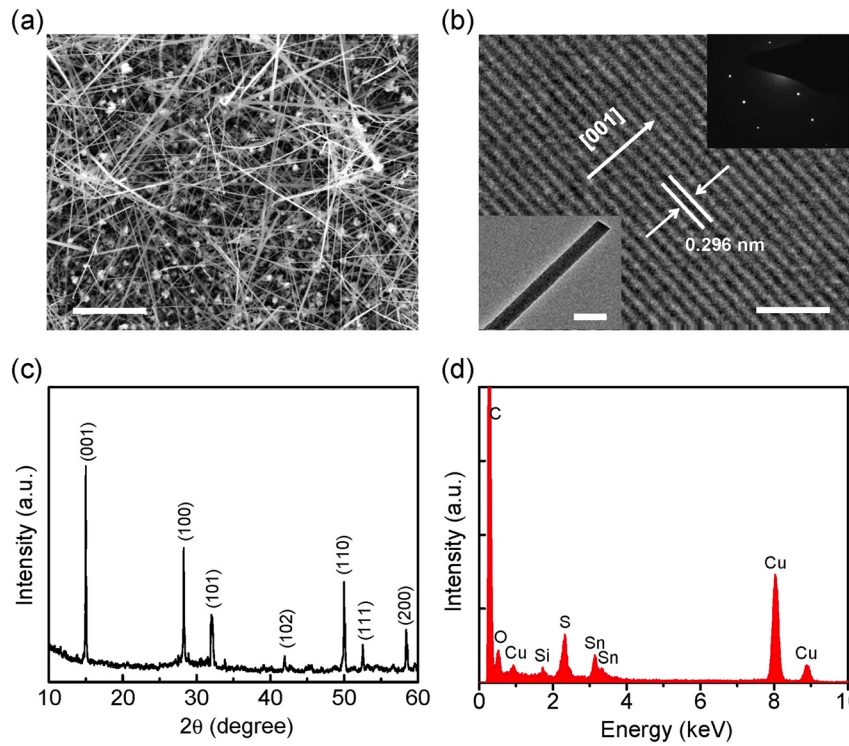
Figure 1: Characterizations of the as-grown SnS₂ NWs. (a) SEM image of SnS₂ NWs. The scale bar is 2 μm. (b) HR-TEM image indicates a single-crystalline structure along the [001] growth direction of the single SnS₂ NW. The lattice distance is ~0.296 nm and the scale bar is 2 nm. The bottom-left inset shows that the diameter of NW is about 40 nm (the scale bar is 50 nm). The top-right inset is the corresponding SAED pattern. (c) XRD pattern of the SnS₂ NWs (JCPDS No. 23-0677). (d) EDS spectrum of the SnS₂ NWs.
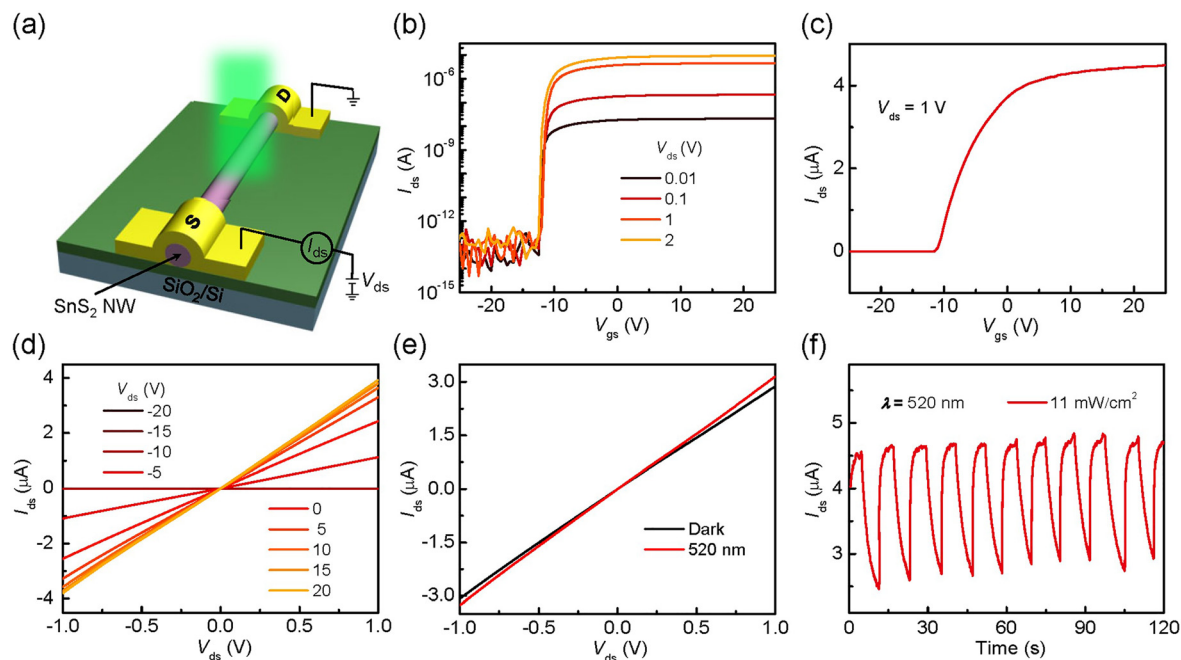

Figure 2: Electrical and optoelectronic properties of the single SnS₂ NW back-gated FET. (a) Schematic diagram of the single SnS₂ NW back-gated FET photodetector. (b) I_{ds}–V_{gs} transfer characteristics of the SnS₂ NW FET at different bias voltages V_{ds}. (c) Linear plot of I_{ds}–V_{gs} transfer characteristics at $V_{ds} = 1$ V. (d) I_{ds}–V_{ds} output characteristics of the device, the back-gated voltage interval is 5 V. (e) I_{ds}–V_{ds} output characteristics of the device in dark and under the illumination of 520 nm laser, measured without additional back-gated voltage. (f) Photocurrent response of the device under optical chopping at $V_{ds} = 1$ V without additional back-gated voltage (520 nm, 11 mW cm^{-2}).
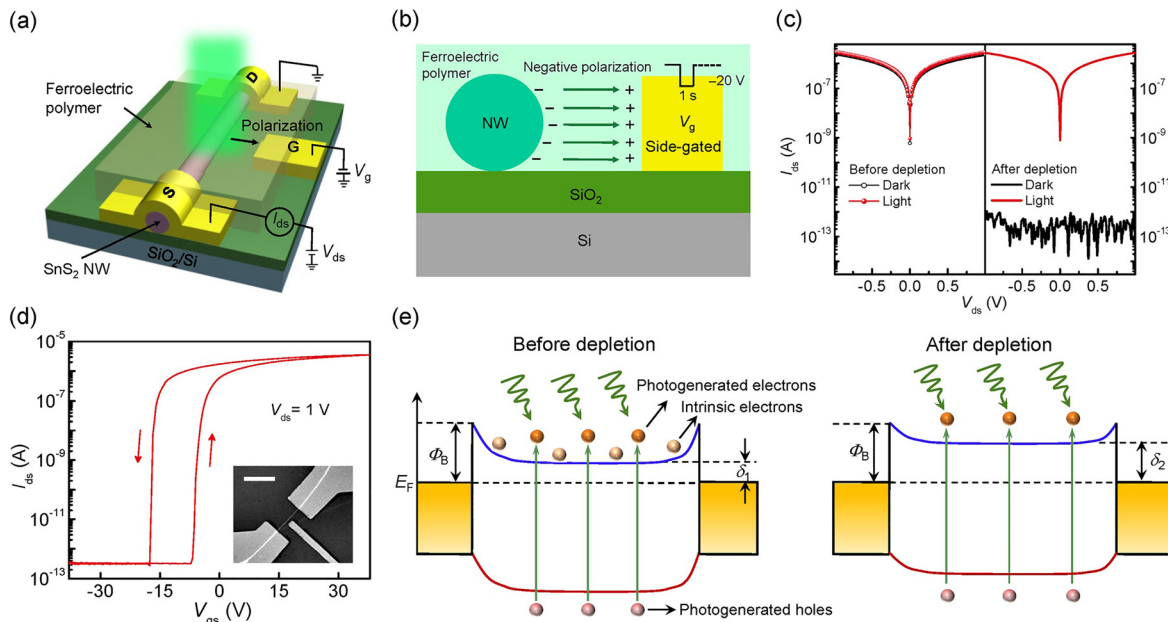
Figure 3: Schematic diagrams, polarization characteristics and energy band diagrams of ferroelectric side-gated single SnS$_2$ NW photodetector. (a) Schematic illustration of ferroelectric side-gated single SnS$_2$ NW photodetector. (b) The cross-sectional structure and schematic diagram of the device in negative polarization state. (c) Before and after being depleted by the ferroelectric polymer film, I_{ds}–V_{ds} characteristics of the device in the dark and upon illumination (520 nm, 11 mW cm^{-2}). (d) I_{ds}–V_{gs} transfer curves of the device with local field regulation by P(VDF-TrFE) ferroelectric polymer and side-gated voltage. The inset is the SEM image of the SnS$_2$ NW side-gated FET. (e) Energy band diagrams before and after depletion. E_C is the minimum conduction band energy, E_V is the maximum valence band energy, E_F is the Fermi level energy, Φ_B is the Schottky barrier height, and δ is the height from bottom of conduction band to the Fermi level energy. The bottom of E_C rises upward and δ increases after being depleted.

other n-type SnS$_2$ nanodevices [14]. The I_{ds}–V_{ds} output characteristics of SnS$_2$ FET are shown in Figure 2d. The linear I_{ds}–V_{ds} curves indicate good Ohmic contacts at the metal/SnS$_2$ interface further demonstrating the n-type semiconducting behavior [13]. The net photocurrent under 520 nm illumination is 0.28 μA at a V_{ds} = 1 V, as shown in Figure 2e. Obviously, the large dark current leads to a low I_{ph}/I_{dark} ratio which deteriorates the detectivity of the photodetectors.

The photoresponse characteristics of SnS$_2$ NW photo-detector without additional back-gated voltage (520 nm, 11 mW cm^{-2}) are displayed in Figure 2f. Due to the surface states and crystal quality, the rise and fall time of SnS$_2$ NW photodetectors are about 1.1 and 4.3 s [4, 28–31]. Further, the SnS$_2$ NW photodetector exhibits a relatively low I_{ph}/I_{dark} ratio because of the large dark current. Therefore, to suppress the dark current we employed P(VDF-TrFE) polymer as side-gate, in which the strong local polarization field can fully deplete the carriers suppressing the dark current. The structure diagram of the device is shown in Figure 3a. The SEM image of a representative side-gated SnS$_2$ NW device is given in the inset of Figure 3d, the distance between the NW and the side-gated electrode is 240 nm. The polarization intensity generated

by ferroelectric polymer films is much higher than that of gate electrostatic field in transistors [31–36]. Figure S1 shows the hysteresis line of P(VDF-TrFE) capacitor, the coercive voltage is about 7.9 V and the remnant polarization value is about 5.2 μC cm^{-2}, indicating the strong polarization performance of ferroelectric polymer [32]. Therefore, the stable residual polarization induced by negative voltage can largely deplete the carriers. Even the negative gate voltage is removed, the device still maintains the depletion state. Figure S2 shows the retention characteristics of the device after depletion. The device remained in the depleted state for more than 60 000 s, indicating that the device can work stably for a long time without additional negative gate voltage. Figure 3d shows the transfer properties of SnS$_2$ NW FETs with local field regulation by P(VDF-TrFE) ferroelectric polymer dielectric and side-gated voltage. The linear curve is shown in Figure S3 in the Supplementary Materials. The hysteresis loops along the counterclockwise direction indicate that the ferroelectric local field is well regulated and has strong residual polarization characteristics [31, 32]. Noted that the dark current is suppressed to 3×10^{-13} A for side-gated voltage less than −17.2 V because of the residual polarization of the ferroelectric polymer film.

The negative polarization can deplete the intrinsic carriers in NW. For example, when a negative voltage of −20 V and pulse width of 1 s is introduced to the side-gated electrode, the ferroelectric polymer film is polarized with polarization direction from NW to the side-gated electrode. So, most free electrons in the SnS$_2$ NW channel were depleted by the ultra-high polarization electrostatic field, as shown in Figure 3a and b. The schematic diagrams of the ferroelectric side-gated SnS$_2$ nanowire structure before depletion and after depletion are shown in Figure S4 in the Supplementary Materials. After the electrons in the NW are depleted, the conduction band energy level rises upward, and the channel current drops below pA, in a depleted state. The energy band diagram before and after depletion is shown in Figure 3e. Because of the residual polarization in ferroelectric polymer, the dark current is largely suppressed and decreased to below 10^{-12} A (Figure 3c), even after removing the side-gated voltage [34]. With reduced dark current, the performance of NW photodetectors was dramatically improved. For example, the I_{ph}/I_{dark} ratio was improved from less than 1 to 10^7 and the photocurrent was also improved from 0.49 to 2.74 μA with the introduction of a strong polarization electric field. The mechanism of polarization-manipulated photodetection is shown in Figure 3e. Before depletion, the dark current comes from the thermionic emission and tunneling of the intrinsic carriers. Under illumination, the photo-generated electron–hole pairs contribute to the photocurrent together with the dark current to form the total channel current. With negative polarization, the electrons in the NW are depleted and the conduction band minimum rises upward, then the channel current under illumination is mainly attributed to the photo-generated electron–hole pairs [6, 34, 35].

Next, the photoresponse of the device with depletion was further characterized. Figure 4a shows the photo-induced I_{ds}–V_{ds} curves of polarization-depleted SnS$_2$ NW photodetectors. The extracted I_{ph} as a function of light intensity is shown in Figure 4b. The results show that the photocurrent I_{ph} obviously depends on the light intensity (P), which can be expressed as [4] $I_{ph} = cP^k$, where k is 0.7 through the fitting of I_{ph}–P curve. These results indicate complicated processes of photo-generated electron–hole generation, capture, and recombination in the SnS$_2$ NW device [4, 7].

To evaluate the conversion efficiency and photoresponse of the SnS$_2$ NW photodetector, the key parameters such as photoconductive gain (G), responsivity (R), and detectivity ($D^\star$) are characterized, and their dependence on the light intensity are also studied, as shown in Figures 4c and 5a. The photoconductive gain G of the device is defined as $G = N_e/N_{ph}$, where N_e and N_{ph}, respectively, represent the electron–hole pairs number and the photons number absorbed by NW in unit time [3, 31]. The G can be defined as $G = (I_{ph}/e)/(PA/h\nu)$ [3, 31], where $h\nu$ is the energy of the incident photon, e is the charge of electron, and A is the effective irradiated region of the photodetector. The effective irradiated region could be estimated through the cross-sectional area of SnS$_2$ NW, which can be expressed as $A = L \times d$, where L is the length of the NW channel, d is the diameter of the NW [3, 31]. The responsivity or sensitivity is also a key parameter expressing the ability of the photodetector to convert light signals into electrical
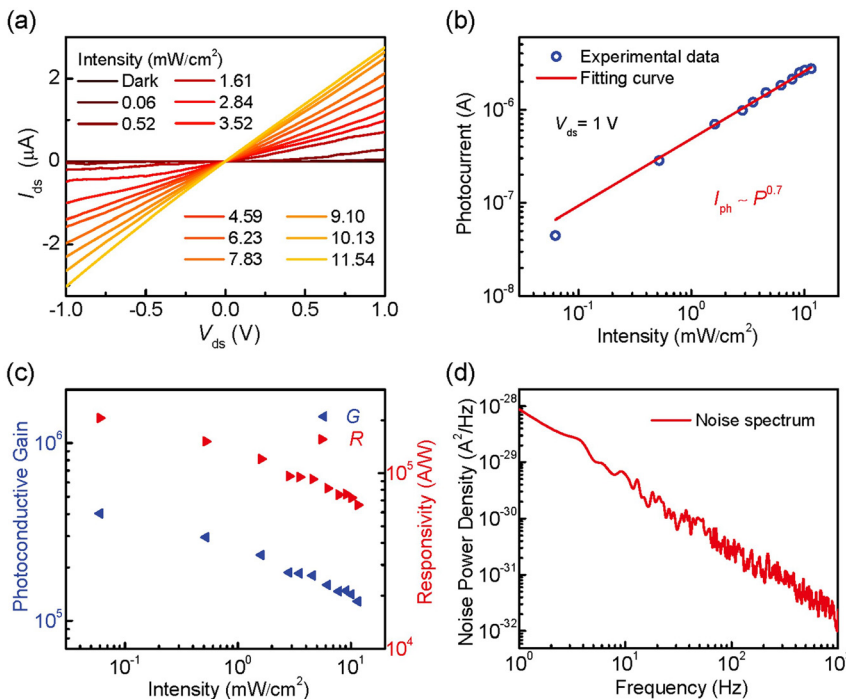

Figure 4: Photoresponse properties and noise power density spectra of ferroelectric side-gated single SnS$_2$ NW photodetector. (a) I_{ds}–V_{ds} characteristics of the photodetector under various intensities (520 nm) after being depleted, without additional gate voltage. (b) Dependence of photocurrent on various intensities, at V_{ds} = 1 V. (c) Dependence of photoconductive gain and responsivity on various intensities, at V_{ds} = 1 V. (d) Noise power density spectra of the device at V_{ds} = 1 V.
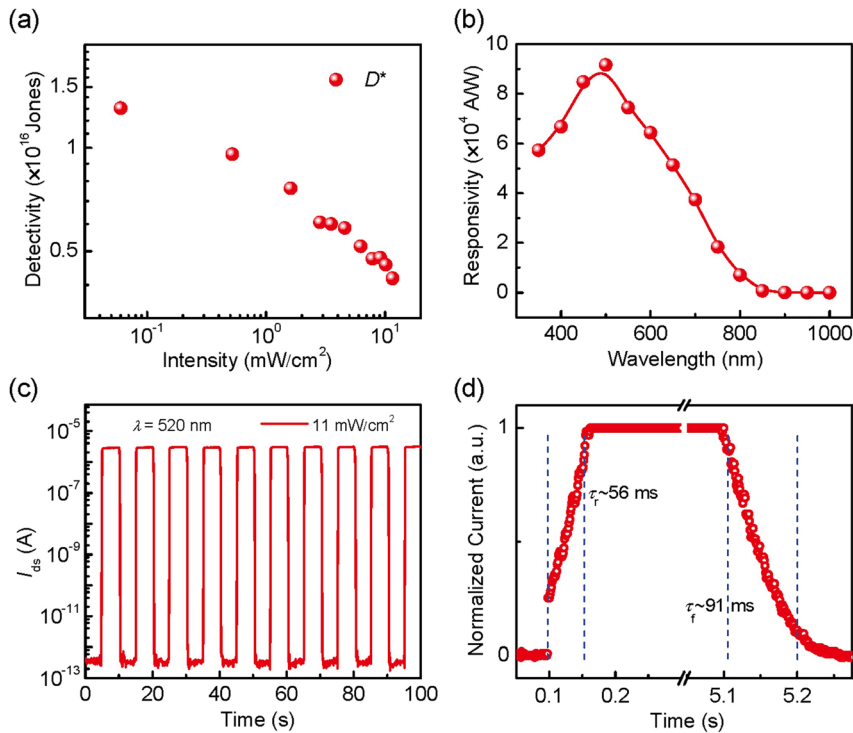
Figure 5: Detectivity, spectral and time response characterizations of ferroelectric side-gated single SnS$_2$ NW photodetector. (a) Specific detectivity of the photodetector under various intensities, at V_{ds} = 1 V. (b) Spectral response of the device at different illumination wavelengths from 350 to 1000 nm under light intensity of 3.8 mW cm^{-2}, V_{ds} = 1 V. (c) Photocurrent response of the device under optical chopping (520 nm, 11 mW cm^{-2}) at V_{ds} = 1 V, without additional gate voltage. (d) Time-resolved photocurrent response of the device.

signals, which can be expressed as the ratio of the output photocurrent signal of the detector to the incident light power, expressed as $R = I_{ph}/(PA)$ [3, 32, 37]. Figure 4c presents the G and R of the photodetector at various light intensities and V_{ds} = 1 V. The results show that the G is 4.0×10^5 and R is up to 2.1×10^5 A W^{-1} under the low light intensity of 0.06 mW cm^{-2}. Obviously, because of the high mobility of the device, the carrier transit time in the channel is short leading to high gain [3, 7]. The specific detectivity represents the minimum detectable signal of the photodetector, which is defined as $D^\star = (AB)^{1/2}/(NEP)$ [3, 38], where B and NEP represent the electrical bandwidth and the NEP. NEP is generally related to three main noise sources, namely shot noise, Johnson noise, and flicker noise (1/f noise) [34, 38]. Noise power density spectra of a single SnS$_2$ NW photodetector was measured by a noise spectrum analyzer at 1 V bias, as shown in Figure 4d. Figure S5 shows the noise power density spectra of the device under different bias voltages. The low-frequency noise characteristics of the device at 0.1 and 1 V bias are close to the background noise at 0 V bias [34]. When the frequency is low, 1/f noise plays a dominant role, thermal noise and shot noise are independent of frequency and are not obviously observed, which is mainly because of the device's low dark current [34, 39].

The NEP can be presented as NEP = $\sqrt{\langle i_n \rangle^2}/R$ [34, 38, 39], where $\langle i_n \rangle^2 = 6.9 \times 10^{-28}$ A^2 is the total noise current power, which is integrated noise power density $S_n(f)$ in the device bandwidth. The flicker noise current of the photodetector $i_n \approx 2.6 \times 10^{-14}$ A.

Figure 5a shows that the $D^\star$ is up to 1.3×10^{16} Jones at a low light intensity of 0.06 mW cm^{-2}. Under the same conditions, $D^\star$ with polarization depletion is at least two orders of magnitude higher than that of device without polarization depletion due to the reduced dark current. The SnS$_2$ NW photodetectors with ultra-high R and $D^\star$ show better performance than other photodetectors based on Tin sulfides SnS and SnS$_2$ nanostructure reported, as shown in Table 1. Noted that the shot noise caused by dark current would be considered as the main factor restricting the device detectivity at a larger frequency range [3]. Therefore, the suppression of dark current is a critical way to improve the detectivity of the device. With ferroelectric polarization to suppress the dark current, the SnS$_2$ NW photodetectors show an ultrahigh detectivity of 1.3×10^{16} Jones.

The spectral response characteristics of SnS$_2$ NW photodetector from 350 to 1000 nm are displayed in Figure 5b. Noted that the device still shows photoresponse even beyond the cut-off wavelength of 590 nm ($E_g \sim 2.1$ eV). The extended detection wavelength may come from the changes of surface electron–hole distribution and band structures induced by a strong ferroelectric polarization field [32, 37]. Figure S5 shows the photoresponse properties of ferroelectric side-gated SnS$_2$ NW photodetector after depletion under deep ultraviolet illumination (280 nm).

Table 1: Comparison of the critical parameters for tin sulfides SnS and SnS$_2$ nanostructure photodetectors.

Photodetectors	I_{on}/I_{off}	Rise time	Fall time	Responsivity (A W^{-1})	Detectivity (Jones)	References
SnS NW	1.5	1.2 ms	15.1 ms	1.6×10^4	2.4×10^{12}	[7]
SnS NB	10^2	36 ms	7 ms	3×10^2	6×10^9	[8]
SnS NS	1.3	5.1 ms	8.8 ms	156	2.94×10^{10}	[9]
SnS$_2$ NS	10^6	22 ms	11 ms	100		[12]
SnS$_2$ NS	10^3	5 μs	7 μs	8.8×10^{-3}	2×10^9	[13]
SnS$_2$ NS	10^2	20 ms	16 ms	261	1.9×10^{10}	[18]
SnS$_2$ NS	2.3	40 ms	80 ms	1.1×10^3	10^{12}	[40]
SnS$_2$ NW	10^7	56 ms	91 ms	2.1×10^5	1.3×10^{16}	This work

NW, nanowire; NB, nanobelt; NS, nanosheet.

The device exhibits ultra-sensitive photoresponse and wider spectrum detection from ultraviolet to near-infrared [32, 36]. The time-resolved photoresponse was conducted under 520 nm illumination, shown in Figure 5c. The SnS$_2$ NW device exhibits good switching periodicity and stability, and the I_{light}/I_{dark} ratio is as high as 10^7. To precisely measure the device's rise and fall times, a digital oscilloscope was applied to monitor fast-changing photocurrent signals [41, 42]. Figure 5d shows the time-resolution photocurrent response, and the rise time and fall time are 56 and 91 ms respectively. The rise and fall time are tens of times faster than those without ferroelectric polarization. The faster response and recovery time exhibit the faster generation and recombination of electron–hole pairs, which may be related to ultra-high ferroelectric polarization local field generated by P(VDF-TrFE) ferroelectric polymer [30, 34, 43].

4 Conclusions

In this work, we demonstrated CVD-grown SnS$_2$ NWs for photodetectors. To reduce the dark current, the ferroelectric side-gate was integrated with SnS$_2$ NW photodetectors. The dark current is significantly suppressed and minimized after depletion through the ultra-high electrostatic polarization, even after removing the side-gated voltage. The ferroelectric side-gated devices show a large photoconductive gain, ultra-high detectivity and responsivity, rapid response speed, and good spectral response characteristics from ultraviolet to near-infrared. This work opens new avenues for ferroelectric-manipulated photodetection technology.

References

[1] X. F. Duan, Y. Huang, Y. Cui, et al., "Indium phosphide nanowires as building blocks for nanoscale electronic and optoelectronic devices," *Nature*, vol. 409, pp. 66–69, 2001.

[2] J. Zhu, Z. F. Yu, G. F. Burkhard, et al., "Optical absorption enhancement in amorphous silicon nanowire and nanocone arrays," *Nano Lett.*, vol. 9, pp. 279–282, 2009.

[3] X. Liu, L. L. Gu, Q. P. Zhang, et al., "All-printable band-edge modulated ZnO nanowire photodetectors with ultra-high detectivity," *Nat. Commun.*, vol. 9, p. 4007, 2014.

[4] N. Guo, W. D. Hu, L. Liao, et al., "Anomalous and highly efficient InAs nanowire phototransistors based on majority carrier transport at room temperature," *Adv. Mater.*, vol. 26, pp. 8203–8209, 2014.

[5] M. Luo, F. Ren, N. Gagrani, et al., "Polarization-independent indium phosphide nanowire photodetectors," *Adv. Opt. Mater.*, vol. 8, p. 2000514, 2020.

[6] Z. H. Wang and B. Nabet, "Nanowire optoelectronics," *Nanophotonics*, vol. 4, pp. 491–502, 2015.

[7] D. S. Zheng, H. H. Fang, M. S. Long, et al., "High-performance near-infrared photodetectors based on p-type SnX (X= S, Se) nanowires grown *via* chemical vapor deposition," *ACS Nano*, vol. 12, pp. 7239–7245, 2018.

[8] X. Zhou, L. Gan, Q. Zhang, et al., "High performance near-infrared photodetectors based on ultrathin SnS nanobelts grown via physical vapor deposition," *J. Mater. Chem. C*, vol. 4, pp. 2111–2116, 2016.

[9] G. Z. Liu, Y. Li, B. Li, et al., "High-performance photodetector based on two-dimensional Tin (II) sulfide (SnS) nanoflakes," *J. Mater. Chem. C*, vol. 6, pp. 10036–10041, 2018.

[10] L. Wu, Z. Xie, L. Lu, et al., "Few-layer tin sulfide: a promising black-phosphorus-analogue 2D material with exceptionally large nonlinear optical response, high stability, and applications

in all-optical switching and wavelength conversion," *Adv. Opt. Mater.*, vol. 6, p. 1700985, 2018.

[11] Y. J. Gong, H. T. Yuan, C. L. Wu, et al., "Spatially controlled doping of two-dimensional SnS$_2$ through intercalation for electronics," *Nat. Nanotechnol.*, vol. 13, pp. 294–299, 2018.

[12] Y. Huang, H. X. Deng, K. Xu, et al., "Highly sensitive and fast phototransistor based on large size CVD-grown SnS$_2$ nanosheets," *Nanoscale*, vol. 7, pp. 14093–14099, 2015.

[13] G. X. Su, V. G. Hadjiev, P. E. Loya, et al., "Chemical vapor deposition of thin crystals of layered semiconductor SnS$_2$ for fast photodetection application," *Nano Lett.*, vol. 15, pp. 506–513, 2015.

[14] H. S. Song, S. L. Li, L. Gao, et al., "High-performance top-gated monolayer SnS$_2$ field-effect transistors and their integrated logic circuits," *Nanoscale*, vol. 5, pp. 9666–9670, 2013.

[15] D. De, J. Manongdo, S. See, et al., "High on/off ratio field effect transistors based on exfoliated crystalline SnS$_2$ nano-membranes," *Nanotechnology*, vol. 24, p. 025202, 2013.

[16] M. S. Balogun, W. T. Qiu, J. H. Jian, et al., "Vanadium nitride nanowire supported SnS$_2$ nanosheets with high reversible capacity as anode material for lithium ion batteries," *ACS Appl. Mater. Interfaces*, vol. 7, pp. 23205–23215, 2015.

[17] H. Y. Sun, M. Ahmad, J. Luo, et al., "SnS$_2$ nanoflakes decorated multiwalled carbon nanotubes as high performance anode materials for lithium-ion batteries," *Mater. Res. Bull.*, vol. 49, pp. 319–324, 2014.

[18] X. Zhou, Q. Zhang, L. Gan, et al., "Large-size growth of ultrathin SnS$_2$ nanosheets and high performance for phototransistors," *Adv. Funct. Mater.*, vol. 26, pp. 4405–4413, 2016.

[19] W. J. Yan, C. Z. Lv, D. Zhang, et al., "Enhanced NO$_2$ sensitivity in Schottky contacted n-type SnS$_2$ gas sensors," *ACS Appl. Mater. Interfaces*, vol. 12, pp. 26746–26754, 2020.

[20] X. D. Cui, W. W. Xu, Z. Q. Xie, et al., "High-performance dye-sensitized solar cells based on Ag-doped SnS$_2$ counter electrode," *J. Mater. Chem. A*, vol. 4, pp. 1908–1914, 2016.

[21] X. Chen, Y. Hou, B. Zhang, et al., "Low-cost SnS$_x$ counter electrodes for dye-sensitized solar cells," *Chem. Commun.*, vol. 49, pp. 5793–5795, 2013.

[22] Y. F. Huang, W. C. Jiao, Z. M. Chu, et al., "SnS$_2$ quantum dot-based optoelectronic flexible sensors for ultrasensitive detection of NO$_2$ down to 1 ppb," *ACS Appl. Mater. Interfaces*, vol. 12, pp. 25178–25188, 2020.

[23] A. J. Khimani, S. H. Chaki, S. M. Chauhan, et al., "Influence of deposition techniques on quality and photodetection properties of tin disulfide (SnS$_2$) thin films," *J. Mater. Sci. Mater. Electron.*, vol. 30, pp. 13118–13133, 2019.

[24] S. K. Panda, A. Antonakos, E. Liarokapis, et al., "Optical properties of nanocrystalline SnS$_2$ thin films," *Mater. Res. Bull.*, vol. 42, pp. 576–583, 2007.

[25] M. Zervos, C. N. Mihailescu, J. Giapintzakis, et al., "Surface passivation and conversion of SnO$_2$ to SnS$_2$ nanowires," *Mater. Sci. Eng. B*, vol. 198, pp. 10–13, 2015.

[26] X. M. Zou, X. Q. Liu, C. L. Wang, et al., "Controllable electrical properties of metal-doped In$_2$O$_3$ nanowires for high-performance enhancement mode transistors," *ACS Nano*, vol. 7, pp. 804–810, 2013.

[27] J. S. Miao, W. D. Hu, N. Guo, et al., "Single InAs nanowire room-temperature near-infrared photodetectors," *ACS Nano*, vol. 8, pp. 3628–3635, 2014.

[28] S. Jeon, S. E. Ahn, I. Song, et al., "Gated three-terminal device architecture to eliminate persistent photoconductivity in oxide semiconductor photosensor arrays," *Nat. Mater.*, vol. 11, pp. 301–305, 2012.

[29] W. J. Luo, Q. C. Weng, M. S. Long, et al., "Room-temperature single-photon detector based on single nanowire," *Nano Lett*, vol. 18, pp. 5439–5445, 2018.

[30] H. L. Wang, F. Wang, H. Xia, et al., "Direct observation and manipulation of hot electrons at room temperature," *Natl. Sci. Rev.*, vol. 8, p. nwaa295, 2021.

[31] D. S. Zheng, J. L. Wang, W. D. Hu, et al., "When nanowires meet ultrahigh ferroelectric field-high-performance full-depleted nanowire photodetectors," *Nano Lett.*, vol. 16, pp. 2548–2555, 2016.

[32] X. D. Wang, P. Wang, J. L. Wang, et al., "Ultrasensitive and broadband MoS$_2$ photodetector driven by ferroelectrics," *Adv. Mater.*, vol. 27, pp. 6575–6581, 2015.

[33] M. Su, Z. Y. Yang, L. Liao, et al., "Side-gated In$_2$O$_3$ nanowire ferroelectric FETs for high-performance nonvolatile memory applications," *Adv. Sci.*, vol. 3, p. 1600078, 2016.

[34] D. S. Zheng, H. H. Fang, P. Wang, et al., "High-performance ferroelectric polymer side-gated CdS nanowire ultraviolet photodetectors," *Adv. Funct. Mater.*, vol. 26, pp. 7690–7696, 2016.

[35] H. H. Fang and W. D. Hu, "Photogating in low dimensional photodetectors," *Adv. Sci.*, vol. 4, p. 1700323, 2017.

[36] X. T. Zhang, H. Huang, X. M. Yao, et al., "Ultrasensitive mid-wavelength infrared photodetection based on a single InAs nanowire," *ACS Nano*, vol. 13, pp. 3492–3499, 2019.

[37] X. Gong, M. H. Tong, Y. J. Xia, et al., "High-detectivity polymer photodetectors with spectral response from 300 nm to 1450 nm," *Science*, vol. 325, pp. 1665–1667, 2009.

[38] J. R. Manders, T.-H. Lai, Y. B. An, et al., "Low-noise multispectral photodetectors made from all solution-processed inorganic semiconductors," *Adv. Funct. Mater.*, vol. 24, pp. 7205–7210, 2014.

[39] S. P. Chang, C. Y. Lu, S. J. Chang, et al., "Electrical and optical characteristics of UV photodetector with interlaced ZnO nanowires," *IEEE J. Sel. Top. Quant. Electron.*, vol. 17, pp. 990–995, 2011.

[40] Y. Fu, G. Y. Gou, X. W. Wang, et al., "High-performance photodetectors based on CVD-grown high-quality SnS$_2$ nanosheets," *Appl. Phys. A*, vol. 123, p. 299, 2017.

[41] H. H. Fang, W. D. Hu, P. Wang, et al., "Visible light-assisted high-performance mid-infrared photodetectors based on single InAs nanowire," *Nano Lett.*, vol. 16, pp. 6416–6424, 2016.

[42] P. Wang, S. S. Liu, W. J. Luo, et al., "Arrayed van der waals broadband detectors for dual-band detection," *Adv. Mater.*, vol. 29, p. 1604439, 2017.

[43] L. Y. Zhang, X. Q. Xiu, Y. W. Li, et al., "Solar-blind ultraviolet photodetector based on vertically aligned single-crystalline β-Ga$_2$O$_3$ nanowire arrays," *Nanophotonics*, vol. 9, pp. 4497–4503, 2020.